

Plasma cavitation in ultraintense laser interactions with underdense helium plasmas

This article has been downloaded from IOPscience. Please scroll down to see the full text article.

2010 New J. Phys. 12 045014

(<http://iopscience.iop.org/1367-2630/12/4/045014>)

View [the table of contents for this issue](#), or go to the [journal homepage](#) for more

Download details:

IP Address: 130.183.90.175

The article was downloaded on 02/06/2010 at 14:40

Please note that [terms and conditions apply](#).

Plasma cavitation in ultraintense laser interactions with underdense helium plasmas

P M Nilson^{1,6,9}, S P D Mangles¹, L Willingale^{1,7}, M C Kaluza^{1,8},
A G R Thomas^{1,7}, M Tatarakis², R J Clarke³, K L Lancaster³,
S Karsch⁴, J Schreiber^{4,5}, Z Najmudin¹, A E Dangor¹
and K Krushelnick^{1,7}

¹ Department of Physics, Imperial College, London SW7 2AZ, UK

² Technological Educational Institute of Crete, Chania, Crete, Greece

³ CLF, Rutherford Appleton Laboratory, Chilton, Didcot, Oxon., UK

⁴ Max-Planck Institut für Quantenoptik, Garching, Germany

⁵ Ludwig-Maximilians-Universität München, Garching, Germany

E-mail: pnil@lle.rochester.edu

New Journal of Physics **12** (2010) 045014 (10pp)

Received 26 November 2009

Published 30 April 2010

Online at <http://www.njp.org/>

doi:10.1088/1367-2630/12/4/045014

Abstract. Plasma cavitation in an underdense helium plasma driven by an ultraintense laser pulse ($I > 10^{20} \text{ W cm}^{-2}$) is studied. Shadowgraphy and interferometry diagnose plasma channel formation as the laser pulse propagates through the underdense plasma. Measurements of the spatially resolved Thomson side-scattered light generated by the intense-driver pulse indicate the transverse and longitudinal extremities of the cavitated regions that form. Multiple laser-driven channels are observed and each is shown to be a source of electrons with energies greater than 100 MeV. Electron cavitation within an ion channel is consistent with the direct laser acceleration (DLA) mechanism that is present.

⁶ Present address: Laboratory for Laser Energetics and Fusion Science Center for Extreme States of Matter, University of Rochester, Rochester, NY, USA.

⁷ Present address: Center for Ultrafast Optical Science, University of Michigan, MI, USA.

⁸ Present address: Institute for Optics and Quantum Electronics, Jena, Germany.

⁹ Author to whom any correspondence should be addressed.

Contents

1. Introduction	2
2. Experimental setup	3
3. Experimental results	4
4. Electron cavitation	6
5. Summary and conclusions	9
Acknowledgments	9
References	9

1. Introduction

Ultraintense laser systems currently generate subpicosecond pulses with vacuum-focused intensities of $I > 10^{21} \text{ W cm}^{-2}$. In this regime, the laser power significantly exceeds the threshold for relativistic self-focusing [1], making it possible to propagate a laser pulse in a plasma channel over many Rayleigh lengths [2]–[15]. Electrons are accelerated in these interactions by relativistic and ponderomotive effects, leading to major potential applications, including compact electron [16]–[19] and ion [20, 21] accelerators, bright hard x-ray sources [22, 23] and advanced inertial fusion schemes, including fast ignition [24].

One method for accelerating electrons in underdense plasmas is the direct laser acceleration (DLA) mechanism [25, 26]. Here the electrons are no longer accelerated by a plasma wave, but by a combination of the laser field and the electromagnetic fields that are generated in the electron-cavitated ion channel that forms. Cavitation arises from the action of the ponderomotive force associated with the focused laser pulse $F_p = -m_e c^2 \nabla(1 + a_0^2/2)^{1/2}$, where the normalized amplitude for the vector potential is given by $a_0 = eE/m_e c \omega_0$, E is the peak laser electric field, m_e is the electron mass and ω_0 is the laser frequency. The transverse ponderomotive force can totally expel electrons from the axis of laser propagation for laser powers exceeding the critical power $P_c = 17(\omega_0/\omega_p)^2 \text{ GW}$, where ω_p is the plasma frequency.

Complete electron cavitation within an ion channel contributes to a transition in the electron acceleration regime to the DLA mechanism. In particular, electron energies of greater than 300 MeV have been observed from ultraintense laser–plasma interactions that are attributed to this mechanism [26]. The onset of DLA also contributes to the generation of strong synchrotron radiation from such interactions [23]. However, direct observation of cavitation at high ratios of P/P_{cr} (i.e. $P/P_{cr} = 100$ –250) has previously not been observed experimentally [26]–[28].

In this work, we report measurements of complete electron cavitation in underdense laser–plasma interactions. Our results demonstrate channel formation and cavitation with shadowgraphy, interferometry, and by imaging the 90° Thomson side-scattered radiation that is generated by the main-driver pulse. It is shown that the high-intensity laser pulse creates multiple channels inside the plasma and self-scatters from electrons in the ponderomotively driven channel walls. At laser powers approaching the PW level, and with laser intensities of $I > 10^{20} \text{ W cm}^{-2}$, complete electron cavitation is shown to play an important role in the underdense laser–plasma interaction.

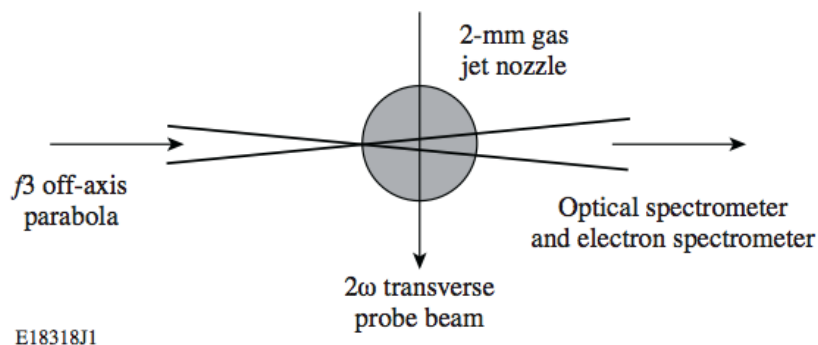


Figure 1. The experimental configuration (top view).

2. Experimental setup

The experiment was carried out on the Vulcan Petawatt laser facility at the Rutherford Appleton Laboratory. The system delivered $\tau_p = 0.65$ ps duration, linearly polarized laser pulses with an energy of up to $E_L = 450$ J at a wavelength of $\lambda_L = 1.054 \mu\text{m}$. A 180-cm-focal-length, $f/3$ off-axis parabolic mirror was used to focus the beam to a vacuum focal spot of $6\text{--}7 \mu\text{m}$ full-width at half-maximum, giving a peak vacuum intensity of $I_L = (4 \pm 1) \times 10^{20} \text{W cm}^{-2}$. Such parameters correspond to a normalized vector potential of $a_0 > 15$. For interactions with plasma electron densities of $n_e = 2 \times 10^{19} \text{cm}^{-3}$, the ratio of the laser power P_L to the critical power P_c for relativistic self-focusing to dominate natural diffractive defocusing is between $P_L/P_c = 100\text{--}250$. The calculated vacuum Rayleigh length $Z_R = \pi\sigma_0^2/\lambda \simeq 30 \mu\text{m}$; σ_0 is the focal-spot radius.

The laser was focused on the edge of a supersonic helium gas jet target that was produced with a 2-mm-diameter nozzle (figure 1). A supersonic gas jet was used to create a reproducible plume of gas in the path of the main interaction beam while maintaining a sharp density profile at the edges of the gas jet. The backing pressure of the gas jet was varied to give plasma electron densities of up to $n_e = 2 \times 10^{19} \text{cm}^{-3}$. Analysis of the wavelength-shifted laser light scattered by the Raman forward-scattering instability provided for a measurement of the plasma electron density during the interaction. The electron density was obtained from the frequency separation of the Raman sidebands to the central laser frequency that occurs at multiples of the plasma frequency.

The interaction was diagnosed with a temporally independent probe beam in a direction transverse to the main interaction (figure 1). The presence of the target plasma induces angular deflections of the probe beam because of spatial variations in the plasmas refractive index. Probe rays are refracted by an angle that is proportional to the refractive index gradient transverse to the initial probe beam direction that is given by $\theta = \int \nabla_{\perp} \eta dl$, where $\eta = (1 - n_e/n_{cr}\gamma)^{1/2}$ is the plasma refractive index, n_{cr} is the critical density, $\gamma = (1 + a_0^2/2)^{1/2}$ is the Lorentz factor for the electrons oscillating in a plane polarized laser field, and dl is a probe ray path element.

The probe beam pulse was derived from the compressed main beam and frequency doubled to 527 nm using a potassium dihydrogen phosphate (KDP) crystal. The accuracy of the probe beam timing with respect to the main interaction beam was comparable to the pulse duration. A $10\times$ -magnified image of the interaction was re-imaged onto two 16-bit charge coupled devices to form shadowgraphy and interferometry diagnostic channels. The interferometer was

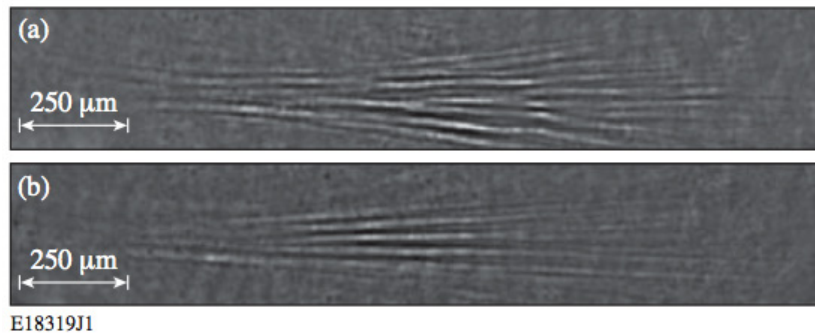


Figure 2. Shadowgrams of helium plasma interactions. (a) $n_e = 1.5 \times 10^{19} \text{ cm}^{-3}$, $P_L = 450 \text{ TW}$ and $t = t_0 + 14 \text{ ps}$. (b) $n_e = 2.5 \times 10^{19} \text{ cm}^{-3}$, $P_L = 450 \text{ TW}$, and $t = t_0 + 10 \text{ ps}$. The laser propagates from the left to right.

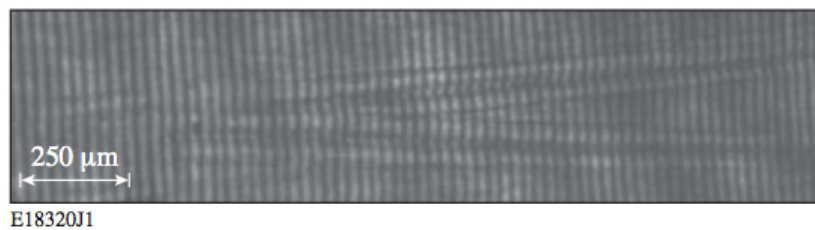


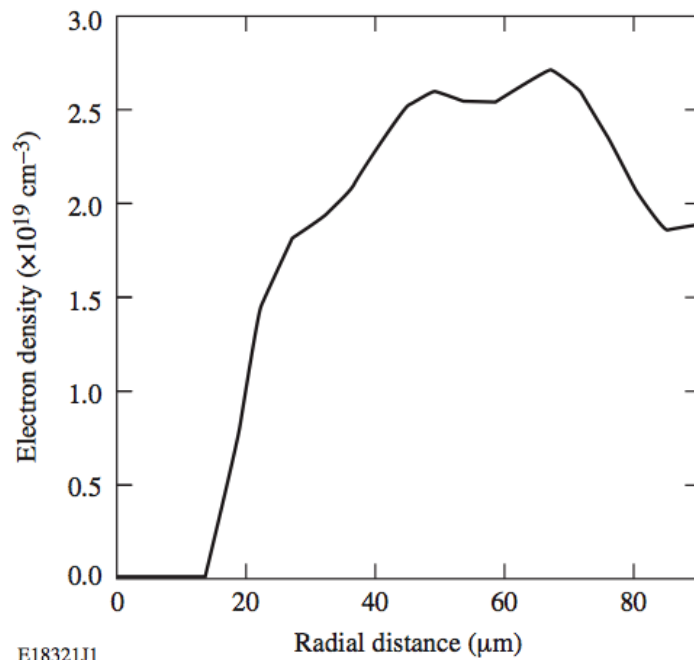
Figure 3. An interferogram of a helium–plasma interaction with $n_e = 2.0 \times 10^{19} \text{ cm}^{-3}$, $P_L = 450 \text{ TW}$, and $t = t_0 + 10 \text{ ps}$.

based on the modified Nomarskii design, which uses a Wollaston prism and a pair of plane polarizers [29]. Various neutral-density filters and an interference filter ($527 \pm 10 \text{ nm}$) were used to reduce the intensity of light that could reach the detectors.

3. Experimental results

Figure 2 shows shadowgrams from laser–plasma interactions with electron densities of $n_e = 1.5 \times 10^{19} \text{ cm}^{-3}$ (figure 2(a)) and $n_e = 2.5 \times 10^{19} \text{ cm}^{-3}$ (figure 2(b)). The images were taken at $t = t_0 + 14 \text{ ps}$ (figure 2(a)) and $t = t_0 + 10 \text{ ps}$ (figure 2(b)), where t_0 is the time at which the high-intensity laser pulse reaches the front edge of the gas jet. The laser pulse propagates around $250 \mu\text{m}$ beyond the laser vacuum focus and breaks up into a number of filaments extending greater than 10 Rayleigh lengths. Density modulations of the filaments, evident from figure 2(a), were probably caused by space-charge-induced ion motion that seeded hosing-type instabilities as the laser pulse propagated in the plasma [30]. Earlier work [14] performed at much lower laser powers ($P_L \simeq 4 \text{ TW}$) observed stable plasma channel formation over 1 mm distances in He plasmas with similar electron densities to those reported here. Little beam filamentation was observed in that work due to significant ($\simeq 60\%$) laser-energy trapping within a single, narrow plasma channel. In contrast, while shot-to-shot fluctuations were observed in the present study, multiple filament-seeded channels are typical of the interactions that were studied, and whole-beam self-focusing leading to single-channel formation was not observed.

The minimum number of filament-seeded channels that was observed corresponds to interactions with initial electron densities of $n_e = 2.0 \times 10^{19} \text{ cm}^{-3}$ (figure 3). Figure 3 shows an



E18321J1

Figure 4. Radial electron-density variation of a laser-generated channel in a helium plasma with an initial electron density $n_e = 2.0 \times 10^{19} \text{ cm}^{-3}$, $P_L = 450 \text{ TW}$ and $t = t_0 + 10 \text{ ps}$.

interferogram of a helium–plasma interaction with $n_e = 2.0 \times 10^{19} \text{ cm}^{-3}$ taken at $t = t_0 + 10 \text{ ps}$. The laser pulse filaments into two distinct regions after the laser–vacuum focus and forms two channels. The dual filamentary structure was consistently observed at these densities and was separated by an angle of approximately 10° . Each channel spanned the length of the 2-mm gas jet and, at this time interval, had radii of around $80 \mu\text{m}$. Channel-formation bifurcation has been observed previously in laser–plasma experiments with 50 fs duration pulses and at lower laser powers ($P_L \simeq 10 \text{ TW}$), and was a result of laser pre-pulse [31]. Laser pre-pulses were observed in that work to split self-guided channels and suppress Raman forward scattering.

The localized fringe shifts in figure 3 show the formation of two channels and their higher electron density walls. The channels appear to form following a propagation length of around $250 \mu\text{m}$ after the laser–vacuum focus. The radial electron-density variation for one of the channels presented in figure 3 is shown in figure 4. The electron-density profile of the cylindrically symmetric channel is shown, with the radial electron density profile being recovered by employing an Abel inversion. The peak electron density in the channel wall was $n_e \simeq 2.6 \times 10^{19} \text{ cm}^{-3}$. An $\sim 25\text{-}\mu\text{m}$ -diameter region on the channel axis was inaccessible to the probe beam because steep electron-density gradients refracted the probe beam out of the acceptance angle of the collection optics.

Electron-beam divergence measurements under similar interaction conditions indicated a finite number of electron beams exiting the plasma. Figure 5 shows various profile images of the electron beam exiting the rear of the gas jet. The measurement was made with a stack of filtered image plates, with each image representing the profile for electrons above a certain cut-off energy. Note that each image is normalized to the peak energy of the given layer. Two high-energy electron beams were observed to exit the plasma with a maximum energy greater

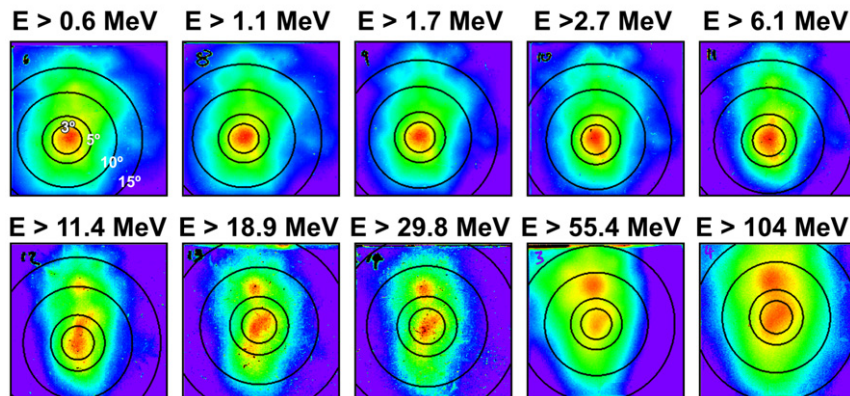
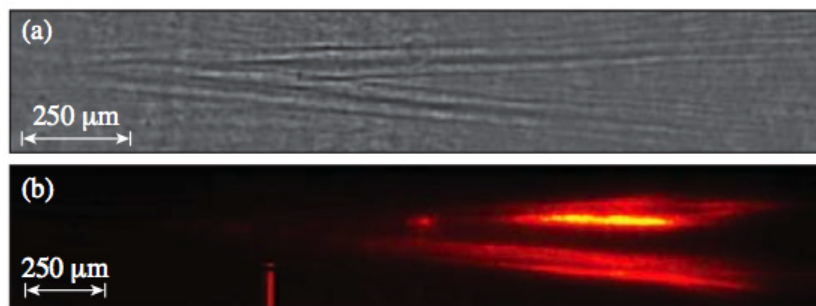


Figure 5. Electron beam profile at $n_e = 2.0 \times 10^{19} \text{ cm}^{-3}$, $P_L = 350 \text{ TW}$. Contours at 3° , 5° , 10° and 15° are shown on each image to give an angular scale. The contours are centered on the principal electron beam axis, i.e. not necessarily the laser axis. Each image shows the profile for electrons above a cut-off energy and is shown normalized to the peak signal for that energy bin.



E18322J1

Figure 6. (a) A shadowgram of a helium plasma interaction with $n_e = 2.0 \times 10^{19} \text{ cm}^{-3}$, $P_L = 450 \text{ TW}$, and $t = t_0 + 10 \text{ ps}$. (b) Time-integrated image of the side-scattered light taken with a camera fitted with a $1.054 \mu\text{m}$ interference filter ($\Delta\lambda = 10 \text{ nm}$). The laser propagates from the left to right.

than 100 MeV. This observation is suggestive of well-defined accelerating structures within the plasma, which is consistent with multiple-channel formation. Indeed, the angular separation of the two electron beams is around 10° , which is consistent with that observed between the two laser-generated channels shown in figure 3.

4. Electron cavitation

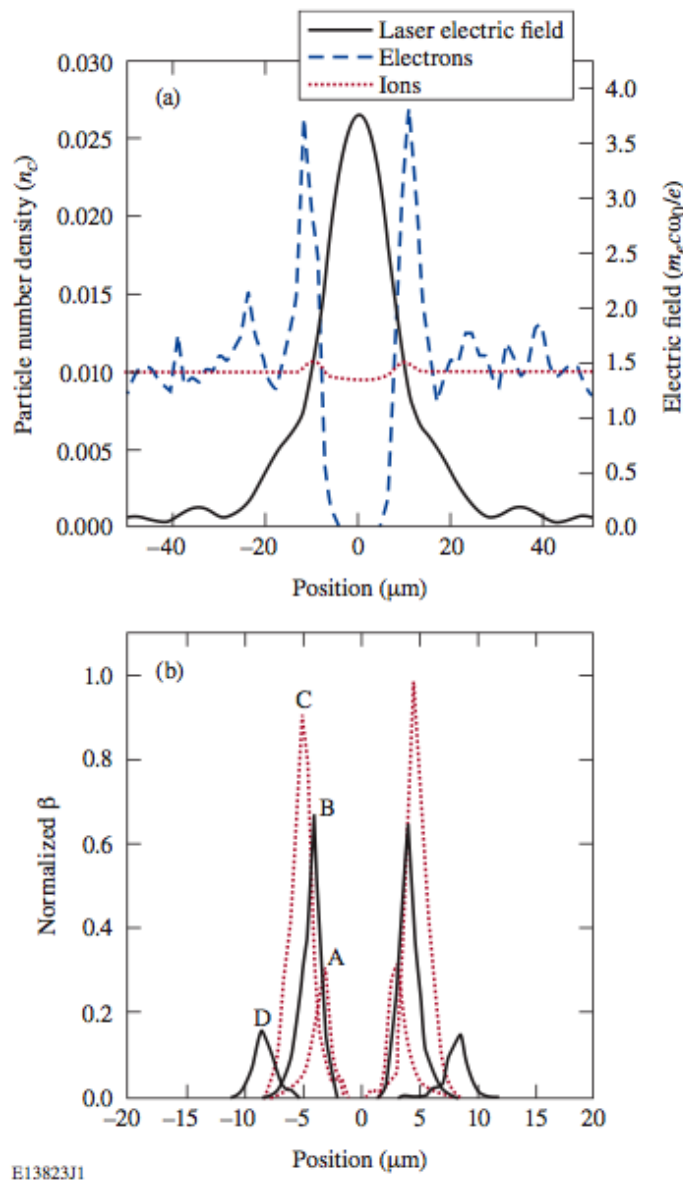
To further diagnose the spatial extent of the plasma channels, Thomson-scattered radiation generated by the intense laser pulse as it propagated through the plasma was imaged in a direction transverse to the laser propagation direction. An image of the time-integrated Thomson-scattered light from an interaction with electron density $n_e = 2.0 \times 10^{19} \text{ cm}^{-3}$ is compared in figure 6 to a shadowgram taken at $t = t_0 + 10 \text{ ps}$ with the same

laser irradiation conditions. An interference filter was used to bandpass light around the fundamental laser wavelength ($\Delta\lambda = 10$ nm) (figure 6(b)). A correlation was observed between the spatial location of the channel walls and the brightest regions of Thomson-scattered light.

The measurement of the Thomson-scattered light can be interpreted as the temporal evolution of the filamentation process of the laser pulse. Thomson-scattered light is generated by the intense laser pulse alone and provides a direct, spatially resolved probe of electrons during the passage of the main driver pulse through the plasma. The temporal resolution of the optical emission is governed by the duration of the laser pulse. Once the laser pulse departs a region of plasma, the Thomson-scattering process terminates. This effect provides information on the presence or absence of electrons in the regions of steepest electron-density gradients that are inaccessible to conventional external optical probing techniques. The image in figure 6(b) resolves for the first time the spatial extent of the cavitation following the passage of an intense laser pulse with $I_L > 10^{20}$ W cm⁻² in an underdense plasma.

Figure 7 demonstrates the cavitation and sidescatter process in a single laser-driven channel with the Osiris PIC code [32]. Simulations are presented with a 2D 3V configuration (two spatial and three momenta coordinates). A stationary box was used to observe the plasma evolution following the passage of a laser pulse with $a_0 = 15$. A density profile for fully ionized helium was modeled with a 0.1 mm ramp to a density of $0.01 n_{cr}$ and was maintained over 0.5 mm, where n_{cr} is the critical density. The linearly polarized laser beam had a Gaussian profile of 0.65 ps duration. The beam was focused to the top of the density ramp and corresponded to a power of 0.4 PW. The computational grid had longitudinal and transverse dimensions of 587 and 168 μ m, respectively. The calculated electron density (black), ion density (red), and laser electric field (blue) at time $t = t_0 + 0.8$ ps are shown in figure 7(a) along a cross section of the computational grid at the top of the density ramp. The head of the laser pulse has ponderomotively expelled electrons from the region of highest laser intensity. Figure 7(b) shows the parameter β as a function of distance along the computational grid, where β is the product of the electron density and the square of the magnitude of the transverse laser electric field for times $t = t_0 + 0.6$ ps (A), $t = t_0 + 0.7$ ps (B), $t = t_0 + 0.8$ ps (C) and $t = t_0 + 1.5$ ps (D). This parameter is proportional to the magnitude of the incoherent Thomson-scattered signal that is generated in the interaction and indicates the spatial extent from which scattered light can be produced.

The absence of laser-light scattering from within the laser-driven channel that forms signifies absence of electrons in this region. This observation is a direct measurement of electron cavitation. Scattering occurs only from the walls of the cavitating ion channel, where the electron density is at a local maximum. This is in contrast to earlier Thomson side-scattered light measurements at lower laser powers where single filamentary structures were observed [14]. The experimental measurements (figures 3 and 6) suggest that the laser pulse does not remain fully constrained by the electron-cavitating channel as it propagates but expands in the lateral dimension. This allows a component of the laser electric field to exist outside of the cavitating region and for Thomson-scattered light to be generated, while the filamented laser pulse still maintains sufficient power to cause cavitation. Once the laser pulse has passed, the scattering process terminates. As a result, there is an inherent temporal resolution associated with the measurement that indicates electron cavitation on a timescale that is of the order of the laser pulse duration. The interplay between the electron-cavitation front and the transverse spatial extent of the self-focusing laser pulse (figure 7(b), A–D) determines the spatial size of the



E13823J1

Figure 7. Particle-in-cell simulation results for a $\tau_p = 0.65$ ps, $P_L = 0.4$ PW laser pulse with $a_0 = 15$ propagating through a helium plasma with density $n_e = 0.01 n_{cr}$. (a) Electron density (black), ion density (red) and laser electric field (blue) along a cross section of the computational grid at $t = t_0 + 0.8$ ps. (b) Variation of β with transverse spatial location, where β is the product of the electron density and the square of the magnitude of the transverse laser electric field between $t = t_0 + 0.6$ ps (A), $t = t_0 + 0.7$ ps (B), $t = t_0 + 0.8$ ps (C) and $t = t_0 + 1.5$ ps (D).

time-integrated Thomson-scattered signal. This effect implies more efficient guiding of the intense driver pulse earlier in the interaction because greater emission is observed at the rear of the gas jet.

Such a picture is consistent with the DLA mechanism that accelerates electrons to greater than 100 MeV in these interactions (figure 5) [26]. The electrons that are accelerated to the highest energy are confined to the cavitating channel by the self-generated quasi-static electric and magnetic fields that form. Strong energy coupling occurs when the frequency of the betatron oscillating electrons is approximately equal to the laser frequency. The cavitation process at these high intensities also leads to a suppression of the forward Raman-scattering instability that limits the contribution of plasma waves to the acceleration mechanism.

5. Summary and conclusions

Measurements have been presented of ponderomotively induced electron cavitation in underdense helium plasmas driven by an ultraintense laser pulse at intensities of $I > 1 \times 10^{20} \text{ W cm}^{-2}$. Spatially resolved Thomson-scattering measurements identify the extent of the cavitating regions. Cavitation is shown to be dynamically significant in these interactions, contributing to the DLA of electrons to energies greater than 100 MeV. Furthermore, cavitation in plasma channels will impact on a variety of ultraintense laser-plasma applications at these high a_0 and P/P_{cr} values, including x-ray production and hole boring.

Acknowledgments

We acknowledge the assistance of the CLF staff and the support of the UK Engineering and Physical Sciences Research Council and AWE plc.

References

- [1] Sun G-Z *et al* 1987 *Phys. Fluids* **30** 526
- [2] Sullivan A *et al* 1994 *Opt. Lett.* **19** 1544
- [3] Borisov A B *et al* 1992 *Phys. Rev. A* **45** 5830
- [4] Sprangle P *et al* 1992 *Phys. Rev. Lett.* **69** 2200
- [5] Durfee C G III and Milchberg H M 1993 *Phys. Rev. Lett.* **71** 2409
- [6] Monot P *et al* 1995 *Phys. Rev. Lett.* **74** 2953
- [7] Clark T R and Milchberg H M 1997 *Phys. Rev. Lett.* **78** 2373
- [8] Wagner R *et al* 1997 *Phys. Rev. Lett.* **78** 3125
- [9] Chen S-Y *et al* 1998 *Phys. Rev. Lett.* **80** 2610
- [10] Clayton C E *et al* 1998 *Phys. Rev. Lett.* **81** 100
- [11] Borghesi M *et al* 1997 *Phys. Rev. Lett.* **78** 879
- [12] Krushelnick K *et al* 1997 *Phys. Rev. Lett.* **78** 4047
- [13] Fuchs J *et al* 1998 *Phys. Rev. Lett.* **80** 1658
- [14] Sarkisov G S *et al* 1999 *Phys. Rev. E* **59** 6
- [15] Matlis N H *et al* 2006 *Nature Phys.* **2** 749
- [16] Tajima T and Dawson J M 1979 *Phys. Rev. Lett.* **43** 267
- [17] Mangles S P D *et al* 2004 *Nature* **431** 535
- [18] Geddes C G R *et al* 2004 *Nature* **431** 538
- [19] Faure J *et al* 2004 *Nature* **431** 541
- [20] Wei M S *et al* 2004 *Phys. Rev. Lett.* **93** 155003
- [21] Willingale L *et al* 2006 *Phys. Rev. Lett.* **96** 245002
- [22] Rousse A *et al* 2004 *Phys. Rev. Lett.* **93** 135005

- [23] Kneip S *et al* 2008 *Phys. Rev. Lett.* **100** 105006
- [24] Tabak M *et al* 1994 *Phys. Plasmas* **1** 1626
- [25] Pukhov A, Sheng Z M and Meyer-ter-Vehn J 1999 *Phys. Plasmas* **6** 2847
- [26] Mangles S P D *et al* 2005 *Phys. Rev. Lett.* **94** 245001
- [27] Mora P and Antonsen T M Jr 1996 *Phys. Rev. E* **53** R2068
- [28] Tzeng K-C and Mori W B 1998 *Phys. Rev. Lett.* **81** 104
- [29] Benattar R, Popovics C and Sigel R 1979 *Rev. Sci. Instrum.* **50** 1583
- [30] Najmudin Z *et al* 2003 *Phys. Plasmas* **10** 438
- [31] Chien T Y *et al* 2004 *Phys. Plasmas* **11** 3
- [32] Fonseca R A *et al* 2002 *Computational Science—ICCS 2002* ed P M A Sloot *et al* (*Lecture Notes in Computer Science*) vol 2331 (Berlin: Springer) p 342